The effect of edge profile on Delta wing flow

Shabudin Bin Mat[1], Richard Green[2], Roderick Galbraith[3], Frank Coton[4]

[1]Faculty of Mechanical Engineering, Universiti Teknologi Malaysia
81110, Johor Bahru, Malaysia
[2,3 & 4] James Watt South Building, Glasgow G12 8QQ, UK

Abstract

This paper presents flow measurements on four delta wing configurations which are differentiated by their leading edge profiles; sharp-edged, small-, medium- and large-radius. The experiments were performed as a part of the European Vortex Flow Experiment-2 campaign. Tests were conducted at speeds of 20.63 m/s and 41.23 m/s representing Reynolds numbers of 1×10^6 and 2×10^6 respectively. In this paper oil flow visualization data are presented for the four wings together with Particle Image Velocimetry results for the large radius wing. The study has identified interesting features of the interrelationship between the conventional leading edge primary vortex and the occurrence and development of the inner vortex on the round-edged delta wings. The effects of Reynolds number, angle of attack and leading-edge radii on both vortex systems are discussed in detail.

*Correspondence address: Tel No: +6075534673, Fax No: +6075566159,
Email address: shabudin@fkm.utm.my

Keywords: Delta wing; primary vortex; inner vortex: leading edge bluntness; Reynolds number; angle of attack

1 INTRODUCTION

The flow on the sharp-edged delta wing **[1]** at a certain speed and angle of attack is characterized by the movement of flow from the lower to the upper surface around the leading edges. Flow separation takes place at the leading edge near to the apex and primary vortices are formed over the upper surface. These vortices have their origins as small shear layers at the leading edges which wrap up in a spiral fashion **[2]**. The leading edge vortices grow in strength and size extending from the apex to the trailing edge. These primary vortices are accompanied by smaller secondary vortices which form outboard of the primary vortices and rotate in the opposite sense. There have been numerous investigations to visualize the three-dimensional flow topology above delta wings such as Nelson and Pelletier **[3]**. Despite extensive experimental investigations, numerical and theoretical models still struggle to predict these complicated flow-fields accurately **[4]**.

The round-edged delta wing exhibits different flow patterns compared with the sharp-edged wing, especially in the region of the leading edge

and the apex. The main difference originates in a region of attached flow covering the wing apex region. The flow exhibits an increased attached flow, the extent of which depends on Reynolds number, angle of attack, Mach number and the leading edge profile itself **[1, 5-8].** International Vortex Flow Experiment 2 (VFE-2), of which the current study was part, represented the first major in-depth study of these type of flows. Several experiments, including surface pressure studies, Particle Image Velocimetry (PIV) and numerical work were performed within VFE-2. The resulting understanding of the flow topology is summarized in Fig.1 **[15]**. Fig.1 showed the pressure sensitive paint and particle image velocimetry velocity contour together with numerical performed on the VFE-2 configurations. These results were well agreed that the primary vortex will only appear at certain chordwise position on the wing as shown in the figure. Fig. 1 also indicates attached flow in the leading edge region with separation and vortex formation occurring further down the wing. Another major difference between this flow and that of the sharp-edged wing occurs at moderate angles of attack when a weak circulation region is formed inboard of the primary vortex. This additional vortical structure, which has its origin at about one-third of the wing chord, provided the incentive for some of the early

investigations of the VFE-2 group. The vortex was termed the ‘inner vortex’ and it is its behavior that is considered herein. Earlier studies have stated that the inner vortex develops on the front part of the wing as a result of a three-dimensional separation bubble transition mechanism **[9]**and **[10]**. The objective of this study was to further investigate the complex interation between separating flow in the leading edge and the formation of the inner vortex inboard of the wing.

2 EXPERIMENTAL METHOD

The 65^{o} delta wing test rig, developed at Glasgow, was constructed to be part of the VFE-2 campaign. To consider the effect of leading edge “bluntness”, four interchangeable leading edges, ranging from sharp to large radius, were made. The wing model had a root chord of 1.059 m and a span of 0.987 m. This produced four wings of identical planform shape, but different leading-edge radius to be wind-tunnel tested. These were one sharp edged-wing and three wings with different ratios of leading-edge radius to the mean aerodynamic chord (designated sharp, small, medium and large radius); the profiles are given in Fig. 2.

The experiments were carried out in the Glasgow 2.65 metre by 2.04 metre closed circuit Argyll wind tunnel which has a maximum speed of

76 m/s **[11]**. Test speeds were 20.63 m/s and 41.23 m/s. These corresponded to Reynolds numbers of 1×10^6 and 2×10^6 (based on mean aerodynamic chord respectively). The model was mounted on a sting (Fig. 3) with a centre of rotation at the half wing root chord. Carbon fibre cladding around the sting was shaped to be compatible with the wing centre body profile (Fig. 3). The angle of attack could be varied from 0 to 30 degrees **[11]**. The set up is shown in Fig. 3 The experiments reported herein include the oil flow visualization and Particle Image Velocimetry (PIV) data.

The oil-flow visualization was carried out for all four wings for angles of attack of $10^o \leq \alpha \leq 27^o$ Reynolds numbers of 1×10^6 and 2×10^6. During the experiment, the angles of attack were varied from the medium angle of attack of 10^o where the inner vortex is well devoloped inboard of the wing to the higher angle of attack of 27^o where it almost disappeared **[9]**and **[10]**. The model blockage ratio was 8.29% at the angle of attack of $\alpha = 27^o$. To record the surfaces flow patterns, a combination of Ondina oil, paraffin and yellow Dayglow powder was applied to the upper surface of the wing. The resultant flow patterns were highlighted by fluorescence from ultraviolet illumination and recorded photographically using a high definition 3008 x 2000 pixel

Nikon D70 digital camera located above the roof of the working sector and orthogonal to the surface for all angles considered. The sequence of images recorded was from the initial to the stabilized oil flow pattern.

The Particle Image Velocimetry (PIV) stereoscopic system was as illustrated in Fig. 3. The PIV images were recorded by two 11 Megapixel LaVision cameras with a pair of 300mm focal-length Nikon lenses. Both cameras were mounted on three-dimensional adjustable tripods located outside the test section on the starboard side of the wing model at suitable angles to the considered laser sheet. The system used to illuminate the droplets in the Argyll tunnel was an Nd: YAG pulse laser of 250 mJ per pulse located under the floor of the wind tunnel. The time separations taken between both laser pulses to illuminate the particles were 20 μsecond and 8 μsecond for experiments at Reynolds number of 1×10^6 and 2×10^6 respectively. The selection of this time separation was based on the light sheet thickness and wind tunnel speed. The seeding material used during the experiments was Ondina oil. The generator was placed behind the main support structure of the test rig throughout the experiments. It would be able to produce droplets of diameter around 2 μmm.

It should be noted here that restricted optical access to the working section dictated that camera 2 was located at an extreme angle and this limited the extent to which focus could be achieved across the entire image plane. This resulted in the creation of some non-physical artifacts in the PIV data. Further details are provided in **[11]**.

3 RESULTS

3.1 Oil Flow Visualization Studies

Fig. 4 highlights typical features of the "established" oil flow topologies for the sharp-edged (Fig. 4(i)) and medium-radius (Fig. 4(ii)) delta wings. On the sharp-edged wing the flow separation is at the leading edge starting in the vicinity of the apex. The free vortex rolls-up to form a primary vortex with separation and attachment lines that are visible on the wing surface. Attached flow may also be observed close to the wing centre line and extending from the apex region to the wing sting interface.

Fig. 4(ii) presents the flow topology of a generic round-edged wing. The apex region appears to be covered by fully attached flow up to a certain chordwise distance. The primary vortex then develops further aft of the

apex and is accompanied by a secondary system evidenced by clear separation and attachment lines (as indicated). Inboard on the wing, another flow structure, as discussed by Hummel **[12]** and Fritz **[13]** is the footprint of the inner vortex.

3.1.1 Leading Edge Bluntness Effect

Fig. 5 shows the flow visualization results obtained at a Reynolds number of 2 million for the four different leading edges at an angle of attack of 13.3^{o}. In all cases, the footprint of a vortical structure may be observed near the leading edge. The secondary separation line also clearly delineates the location of the primary and secondary vortex. The first obvious feature is that the primary vortex structures on the medium-radius and large-radius wings no longer begin at the apex as they do for the sharper leading edges .

There is also some evidence of an additional structure, as reported by Hummel **[12]**, inboard of the primary vortex on all of the round-edged wings. That structure becomes more distinct for increasing leading edge radius. It also appears that, increasing the leading edge bluntness moves the starting point of this inner vortex further downstream.

On the small-radius wing, the inner vortex is initiated closer to the apex of the wing compared with the more rounded wings. In fact, the spanwise location and extent of the inner vortex are significantly influenced by the leading-edge bluntness. Increasing bluntness moves the vortex separation line outboard and enlarges the physical size of the structure.

As the bluntness increases, the primary separation on the rounded edges is not fixed to the leading edge as it is on the sharp-edged wing. Rather, the primary separation occurs close to the leading edge after a short run of attached flow in the vicinity of the leading edge **[14]**. This both delays the formation of the primary vortex and reduces its strength. Thus, on the small-radius wing, the primary vortex is weaker than on the sharp-edged wing and less circulation is fed into the inner vortex that forms close to the center-line of the wing. With increasing bluntness, separation is delayed further, particularly in the apex region, and so the formation of both the inner and primary vortices is delayed. As the apex of the primary vortex moves downstream, more circulation is fed into the inner structure that consequently grows in size relative to the other vortex structures.

3.1.2 Reynolds Number Effects

The effect of Reynolds number may be illustrated by comparing the flow patterns at 1.0 and 2.0 million; as depicted in Fig 6. This Figure is for the medium-radius wing at 13.3^{o} angle of attack.

At $R_{mac}=2x10^{6}$ the vortex system appears to originate at approximately 30% of the root chord. Ahead of this, there is no evidence of vortical flow in the oil pattern. This is entirely consistent with previous experimental and computational observations on the same wing geometry [1, 5-8]. In contrast, at $R_{mac}=1x10^{6}$, there appears to be continuity of the primary vortical structure almost to the apex of the wing. Closer examination of the dark region inboard of the secondary separation line shows that it has a distinct bend at about 20-30% of the root chord. The secondary separation line itself becomes indistinct at this point. It is likely that this location is, in fact, the origin of the primary vortex on the wing. Upstream of this, laminar separation is initiated near the leading edge but the shear layer does not roll up into a vortical structure. Instead, the shear layer undergoes transition and reattaches close to the leading edge, leaving the footprint of a laminar separation bubble. This phenomenon appears to occur on the two larger-radius wings at 1 million Reynolds number.

Once initiated, the primary vortex sits closer to the leading edge at the higher Reynolds number. Consistent with this, examination of the inboard portions of the wing shows that the inner vortical structure is initiated slightly closer to the apex and has a greater spanwise extent at the higher Reynolds number.

Fig. 7 shows surface oil flow patterns at Reynolds numbers of $1x10^6$ and $2x10^6$ for the large-radius wing for an angle of attack of $\alpha = 10^o$. The flow pattern at $1x10^6$ exhibits some similarities with the corresponding image for the medium-radius wing. In this case, the primary vortex appears to be initiated further downstream at 50% of the root chord position. Ahead of this, the oil flow trace at the wing leading edge is aligned to the mean flow direction indicating that a vortical structure is not present. A primary vortex is not obvious in the characteristics of the flow pattern at $2x10^6$. An attached flow region aligned with the mean flow exists in the vicinity of the leading edge extending from the apex almost to the trailing edge. This region appears to be truncated by a separation front that becomes increasingly close to the leading edge on aft portions of the wing. The orientation of the oil flow towards the leading edge inboard of this separation front suggests that a weak vortical structure may have formed. This appears to originate

somewhere between 40 and 50% of the wing chord. In fact, a closer examination of the leading edge area near to the trailing edge suggests that a very weak primary vortex is present. In this region, the ratio of the leading-edge radius to the wing span is small increasing the relative sharpness of the profile to the flow. Additionally, the curvature of the trailing edge increases the local angle of attack in the region to promote the primary separation.

3.1.3 Angle of attack effect

Fig. 8 illustrates the variation in the flow pattern on the large-radius wing for six incidences from 10º to 23º. The flow for $\alpha = 10^{o}$ was discussed in the previous section. By $\alpha = 13.3^{o}$, a primary vortex structure has clearly formed on the wing, originating at around 40% of the root chord, with the inner structure apparently originating just ahead of this. In general, the figure shows the progressive movement, with increasing incidence, of the origin of the primary vortex from about 40% of the root chord location towards the wing apex. At $\alpha = 23^{o}$ the primary vortex structure appears to originate close to the apex and extends to the trailing edge.

In Fig. 8, the inboard vortical structure is distinct and extensive at low and moderate angles of attack but appears considerably weakened and

spatially constrained at the highest angle of attack. This may be observed by the inboard shifting of the inner vortex separation line, with increasing incidence and the subsequent strengthening of the vortex. The forward movement of the origin of the inner vortex with increasing incidence may also be observed. Additionally, the lateral extent of the inner vortex is reduced with the upstream progression of the primary vortex. In fact, at moderate α, the upstream progression of the primary vortex compresses the inner vortical structure to the wing centre line.

The simultaneous appearance of the primary vortex and the inner vortex at $\alpha = 10^{o}$ would be consistent with the proposition that the separated flow only rolls-up to generate a spinning vortex inboard on the wing once it interfaces with the primary vortex. This is not the explanation from Hummel and Luckring **[15]**. They suggested that the inner vortex develops from a three dimensional laminar bubble type separation upstream on the wing. At higher angles of attack, the flow in the leading edge region behaves similarly to the behavior observed on the sharp leading edged wing.

3.2 PIV Results

PIV experiments were performed on the large-radius wing at both 1 x 10^6 and 2 x 10^6 Reynolds number. Measurements were made on a fixed measurement plane located midway between the apex and the trailing edge and on the port side of the wing at model angle of attack of $\alpha = 15^o$. Fig. 9 shows the time averaged planar velocity distributions at the two Reynolds numbers in a cross-flow plane extending from approximately y = -40 mm to 100 mm, where y = 0 at the leading edge and the inboard direction is positive. The colour contours in the figure represent the magnitude of the through-plane velocity in the streamwise direction and the position of the wing is drawn onto the figure for clarity.

At a Reynolds number of 1 x 10^6 the primary vortex core location is visible at a height of about 20 mm from the wing surface and is centered at about 65 mm from the leading edge. At 2 x 10^6 Reynolds number (shown in fig. 9 (ii)); the primary vortex is again centered at a height of about 20 mm above the wing surface but, this time, is only 60 mm inboard of the leading edge. This is consistent with the earlier discussion in relation to Fig. 6.

The corresponding time-averaged vorticity distributions for the two cases presented above are given in Fig. 10. Negative vorticity appears in the primary vortex region, and the high negative vorticity coincides with the region of the vortex centre. The primary vortex is slightly larger at the lower Reynolds number which is consistent with the greater ability of the turbulent boundary-layer to endure the adverse pressure gradient at higher Reynolds so delaying the growth of the primary vortex.

Fig. 11 shows the time averaged velocity and vorticity distributions for the large-radius wing from y = 40 to 240 mm at a Reynolds number of 2 x 10^6. In Fig. 11 (i)), the primary vortex is located at the very left of the image. Another vortical structure is evident further inboard at around y = 160mm. This additional structure, is the inner vortex. The structure is particularly clear in Fig. 11 (ii)) that depicts the corresponding vorticity distribution. As expected the inner vortex is considerably weaker and more diffuse than the dominant primary vortex. Interestingly, the large area of positive vorticity at around y = 65 to y = 100 mm appears to be a secondary off-surface structure associated with the interaction of the two co-rotating vortices.

4 CONCLUSION

In this paper, wind tunnel data have been presented for four identical delta-wing planform configurations, differentiated by their leading edge profiles; sharp-edged, small-, and medium- and large-radius. The finite radius on the leading edge of the wing influences both the formation of the primary vortices and the nature of the flow on the inboard sections of the wings. In particular, an additional co-rotating vortex structure is observed inboard of the primary vortex system whose formation arises from the interaction of the delayed separating boundary layer in the apex region of the wing with the primary vortex system. The results presented here show that the formation of primary vortex is very much dependent on the leading edge bluntness, Reynolds number and angle of attack. An increase in leading edge bluntness and Reynolds number delays the formation of the primary vortex towards aft portions of the wing. The results also show that, as the leading edge radius increases, the magnitude of the primary vortex decreases but the magnitude of the inner vortex increases. PIV and oil flow visualization results show that the strength and location of the inner vortex is strongly dependent on Reynolds number with a stronger and more extensive vortex structure evident at higher Reynolds number. The oil flow and PIV results

obtained in this work also strongly indicate that the roll-up of the inner vortex is independent of a separation bubble being formed but arises from the complex interaction between separating flow in the apex region and the primary vortex.

ACKNOWLEDGEMENT

European VFE-2 Working Group and the first author wishes to thank Universiti Teknologi Malaysia for the scholarship support.

REFERENCES

1. **Hummel, D**. "Effects of Boundary layer Formation on the vortical Flow above Slender Delta Wings. RTO specialist Meeting on Enhancement of NATO military Flight Vehicle Performance by Management of Interacting Boundary Layer transition and Separation." Meeting Proceedings RTO-MP-AVT-111. 2004.
2. **Gad-El-Hak, M.** and **Blackwelder**, R.F. "The discrete Vortices from a Delta Wing". Technical Report 1985. Vol 23, 961-962. 1985.
3. **Nelson, R.C.** and **Pelletier, A.** "The Unsteady Aerodynamics of Slender Wings and Aircraft Undergoing Large Amplitude

Maneuvers". Progress in Aerospace Science. Vol 39. Page 185-248. 2003.

4. **Drikakis, D., Li, N., Turner, J.T., Jaworski, A.J.** and **Wood, N.** "Highly Swept Leading Edge Separations." MSTTAR DARP Report. 2003.
5. **Hummel, D.** "The Second International Vortex Flow Experiment (VFE-2): Objectives and Present Status." 25th AIAA Applied Aerodynamics Conference. AIAA 2007-4446. 2007.
6. **Chu, J.** and **Luckring, J.M.** "Experimental Surface Pressure Data Obtained on 65^0 Delta Wing across Reynolds Number and Mach number Ranges." NASA Technical Memorandum 4645. 1996.
7. **Luckring, J.M.** "Reynolds Number and leading-Edge Bluntness Effects on a 65^0 Delta Wing." AIAA-2002-0419.2002.
8. **Luckring, J.M.** "Reynolds Number, Compressibility, and Leading Edge Bluntness Effects on Delta Wing Aerodynamics." 24th International Congress of the Aeronautical Sciences. 2004.
9. **Hummel, D.** "Chapter 17 – The International Vortex Flow Experiment 2 (VFE-2): Objectives and Overview." RTO-TR-AVT-113. 2008.

10. **Hummel, D.** "Chapter 35 – Final Results of the International Vortex Flow Experiments – Résumé and Outlook". RTO-TR-AVT-113. 2008.

11. **Mat, S.** "The Analysis of Flow on Round-Edged Delta Wings. PhD dissertation", University of Glasgow, United Kingdom. 2010.

12. **Hummel, D.** "The Second International Vortex Flow Experiment (VFE-2): Objectives and First Results". Proc.ImechE Vol. 220 Part G: J. Aerospace Engineering. 2006.

13. **Fritz, W.** "Chapter 25 – Numerical Solutions for the VFE-2 Configurations on Structured Grids at EADS-MAS, Germany." RTO-TR-AVT-113. Page 25-1 – 25-21.2008.

14. **Peake, D.J.** and **Tobak, M.** "Three-Dimensional Interactions and Vortical Flows with Emphasis on High Speeds." AGARD-AG-252. 1980.

15. **Luckring, J.M.** and **Hummel, D.** "Chapter 24 – What Was Learned From The New VFE-2 Experiments." RTO-TR-AVT-113.2008.

LIST OF SYMBOLS:

α Angle of Attack

c_r Wing root chord

r_{LE}/c Leading edge radius to wing chord ratio

R_{mac} Reynolds number at mean aerodynamic chord

t/c_r Wing thickness to wing chord ratio

u Velocity component in plane y-z

x Coordinate set parallel with the flow direction/chordwise

x/c_r Chordwise distance from the Apex

y Coordinate set perpendicular with the flow direction

z Coordinate set perpendicular with x-y plane

λ_x Vorticity in s^{-1}

Λ Delta wing sweep angle

Figure Captions

Fig. 1 Comparison of experimental measurements and a numerical solution of the flow above a blunt leading edge wing for Mach number 0.4, $R_{mac} = 3 \times 10^6$ and $\alpha = 13^o$ (Taken from Ref. [9]).

Fig. 2 The geometry of original NASA delta wing showing, i) the interchangeable leading edges & ii) a contour of leading edge profiles for all wings (Taken from Ref. [6])

Fig. 3 Stereoscopic PIV arrangement in the Argyll low speed tunnel

Fig. 4 Flow topology of the sharp-edged and medium radius delta wing ($\alpha = 13.3^o$)

Fig. 5 Comparison of oil flow topology for the; a) Sharp-edged, Small, Medium & Large radius wings at $R_{mac} = 2 \times 10^6$ & $\alpha = 13.3^o$

Fig. 6 Comparison of oil flow patterns for the medium-radius configuration at a) $R_{mac} = 1x10^6$ and b) $R_{mac} = 2x10^6$ & $\alpha = 13.3^o$

Fig. 7 Comparison of oil flow patterns for the large-radius configuration at a) $R_{mac} = 1x10^6$ and b) $R_{mac} = 2x10^6$ & $\alpha = 10^o$

Fig. 8 Flow topology images for the large-radius configuration at $R_{mac} = 2x10^6$ and angle of attack = 10^o, 13.3^o, 15^o, 17^o, 20^o and 23^o

Fig. 9 Velocity distributions at the mid-chord of the large-radius wing in the leading-edge region at Reynolds numbers of 1 and 2×10^6 & $\alpha = 15^o$.

Fig. 10 Vorticity field at the mid-chord of the large-radius wing in the region of the leading-edge at Reynolds numbers of 1 & 2 x 10^o & $\alpha = 15^o$

Fig. 11 Velocity field and Vorticity at the mid-chord of the large-radius wing inboard of the leading edge at a Reynolds number of 2 x 10^6 & $\alpha = 15^o$

Figures

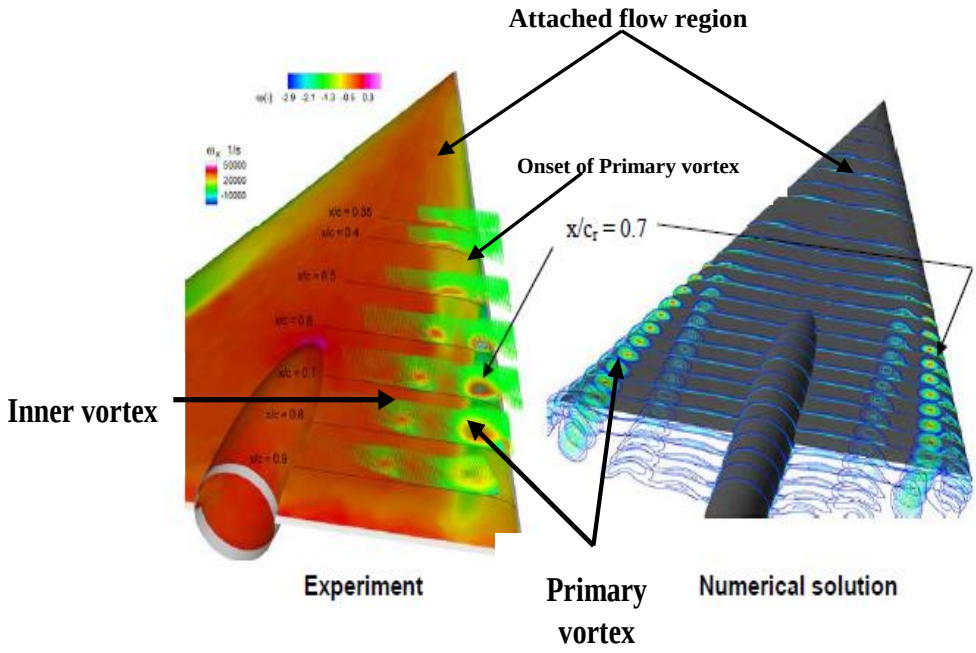

Fig. 1

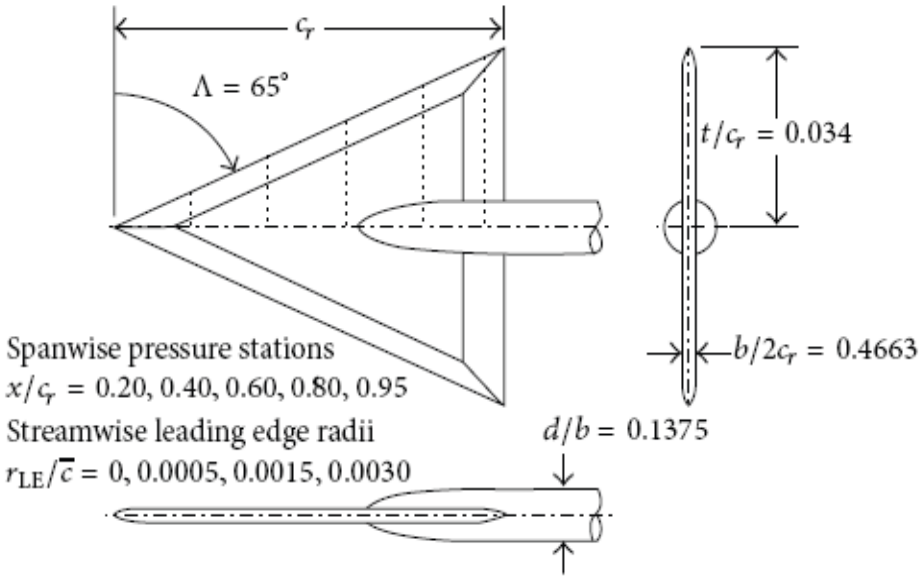
c_r
$\Lambda = 65^\circ$
$t/c_r = 0.034$
$b/2c_r = 0.4663$
Spanwise pressure stations
$x/c_r = 0.20, 0.40, 0.60, 0.80, 0.95$
Streamwise leading edge radii
$r_{LE}/\bar{c} = 0, 0.0005, 0.0015, 0.0030$
$d/b = 0.1375$

i)

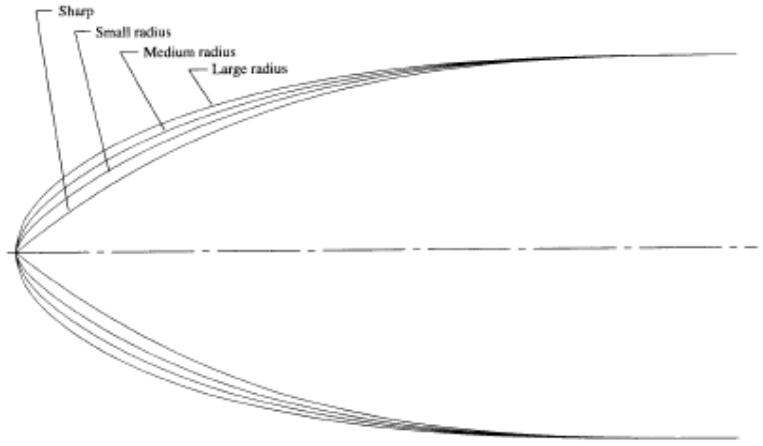
Sharp
Small radius
Medium radius
Large radius

ii)

Fig. 2

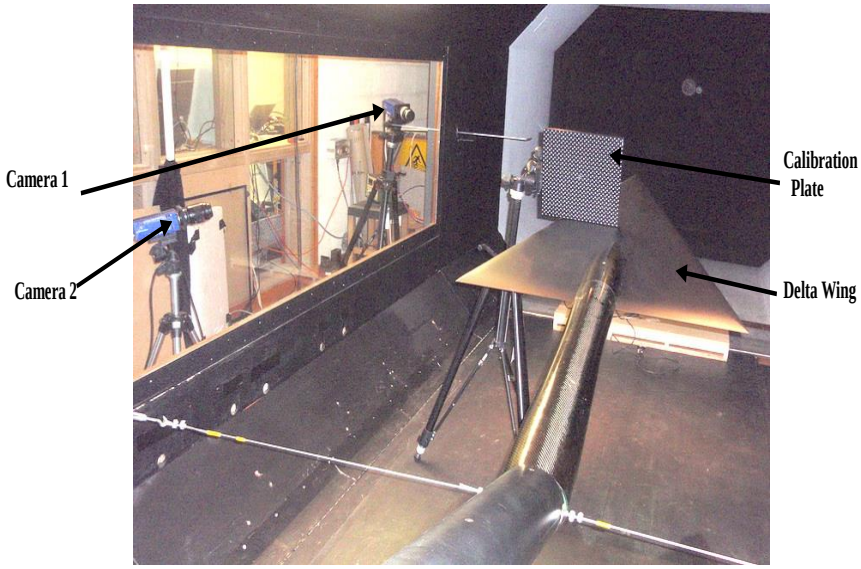

Fig.3

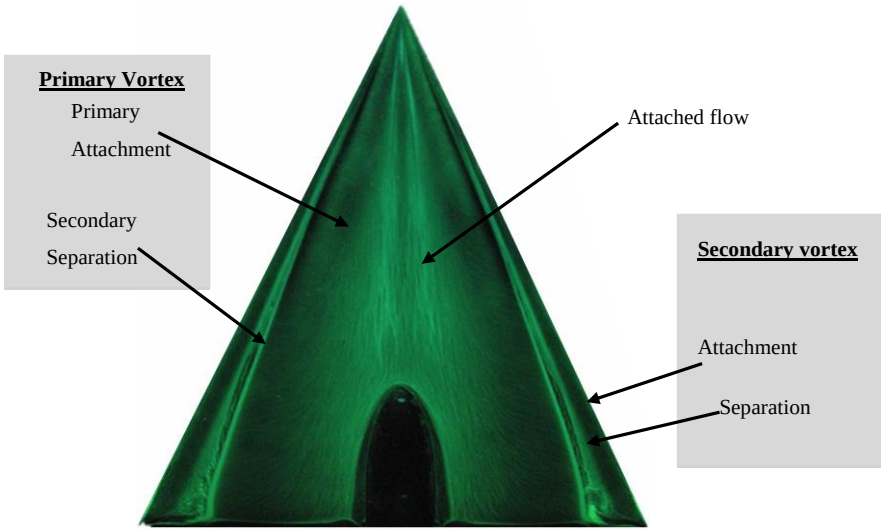

i) Flow topology of the sharp-edged delta wing (α =13.3^o)

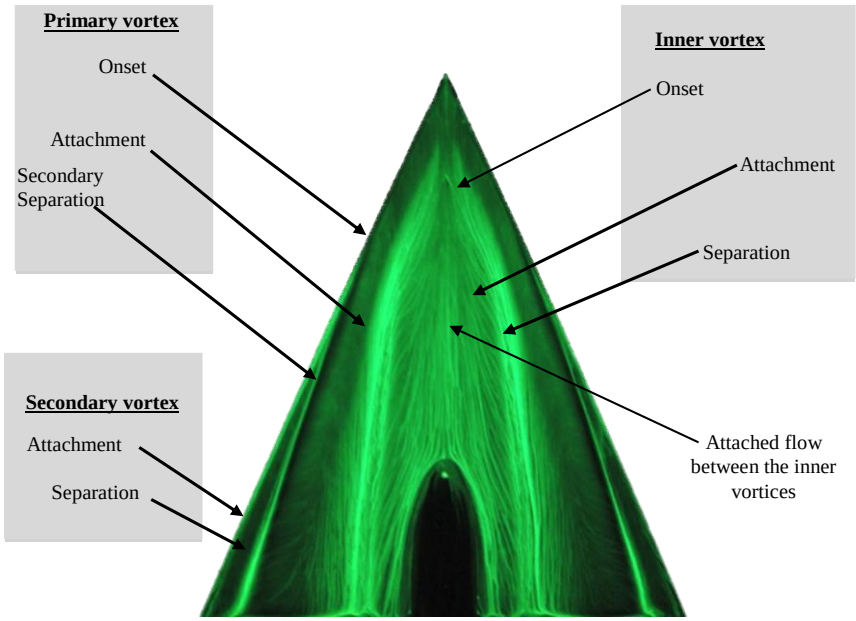

ii) Flow topology of the medium radius delta wing (α =13.3^o)

Fig. 4

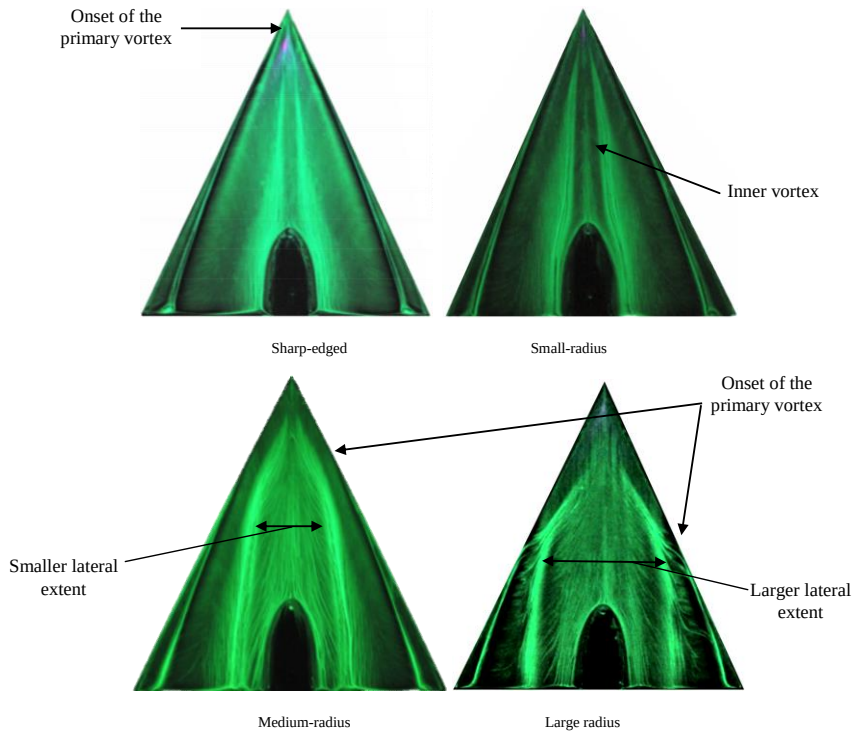
Onset of the primary vortex
Inner vortex
Sharp-edged
Small-radius
Onset of the primary vortex
Smaller lateral extent
Larger lateral extent
Medium-radius
Large radius

Fig. 5

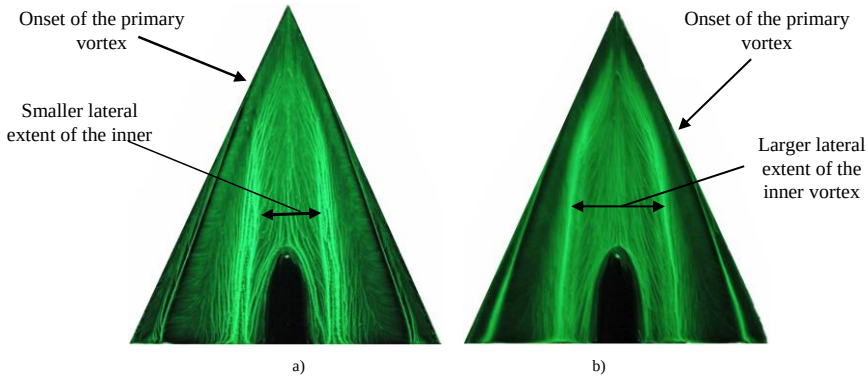
Onset of the primary vortex
Smaller lateral extent of the inner
Onset of the primary vortex
Larger lateral extent of the inner vortex
a)
b)

Fig. 6

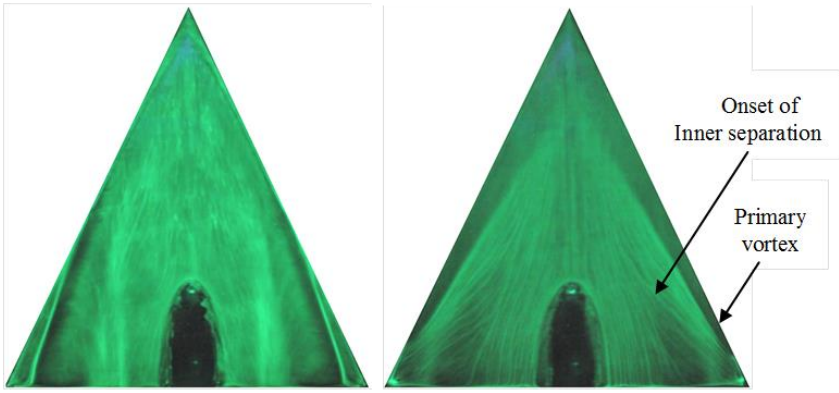
Onset of
Inner separation
Primary
vortex
a)
b)

Fig. 7

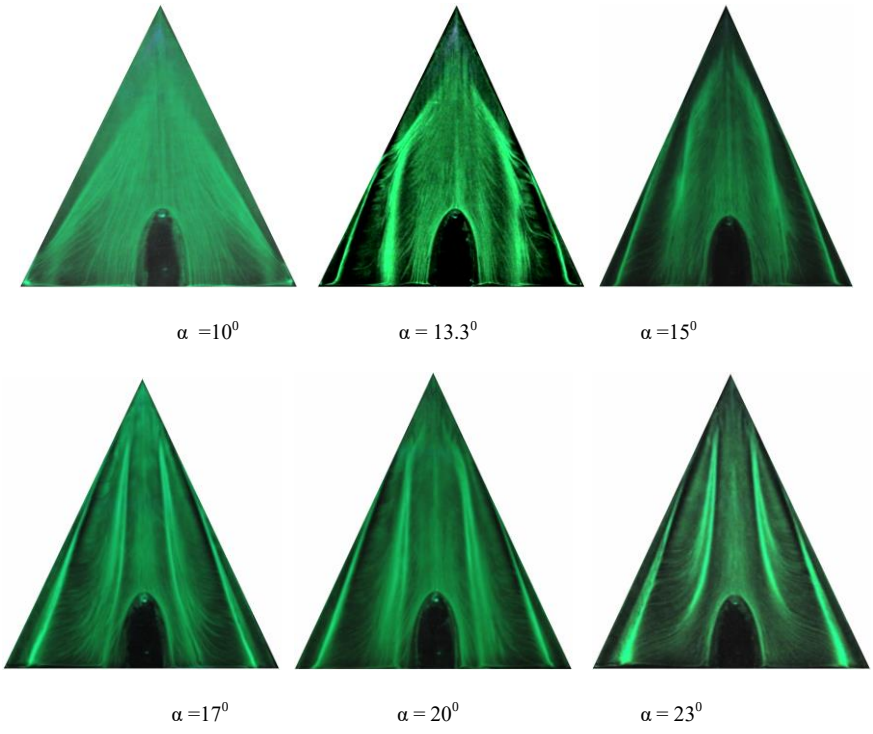
α =10⁰
α = 13.3⁰
α =15⁰
α =17⁰
α = 20⁰
α = 23⁰

Fig. 8

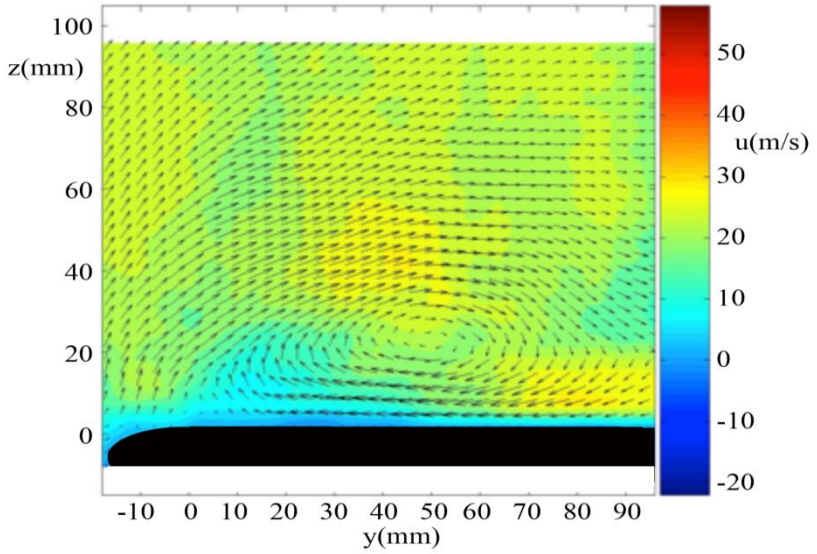

i) 1×10^6

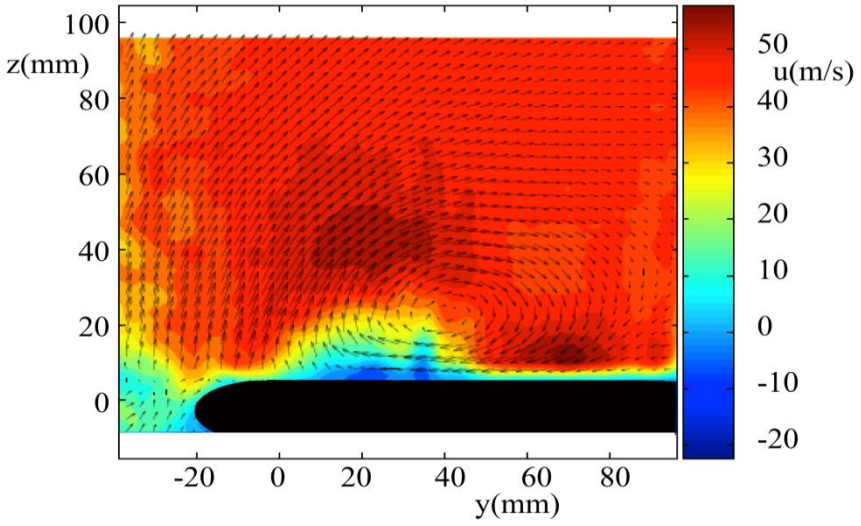

ii) 2×10^6

Fig. 9

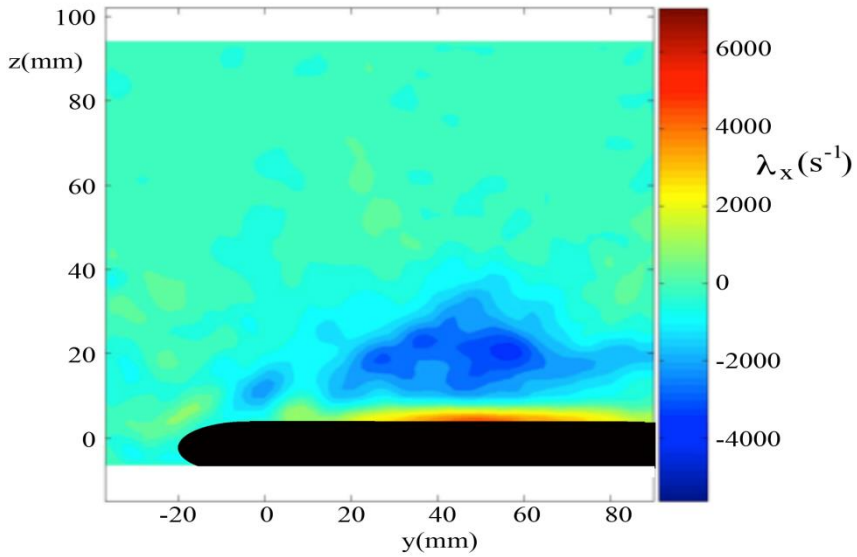

i) 1x 10^6

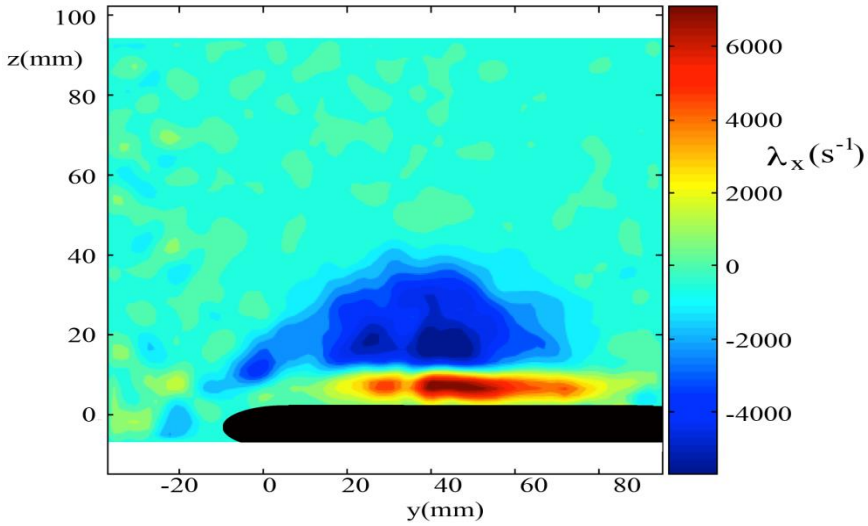

ii) 2 x 10^6

Fig. 10

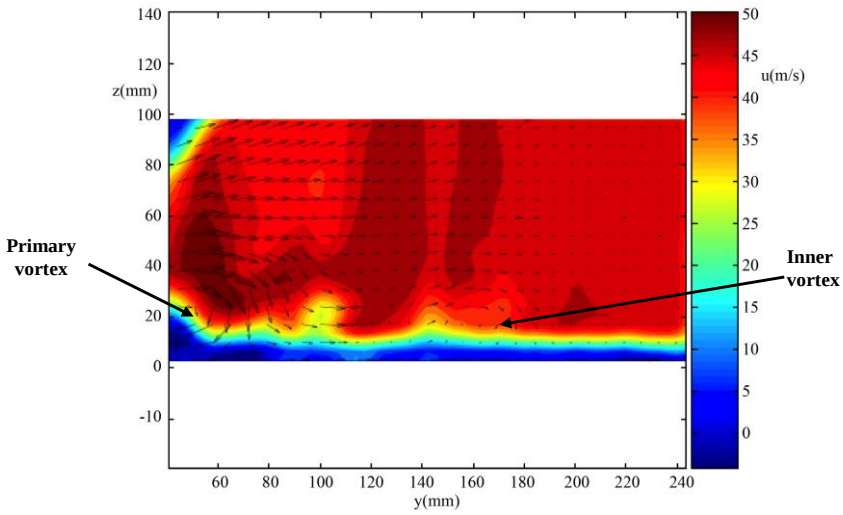

i) Velocity distribution

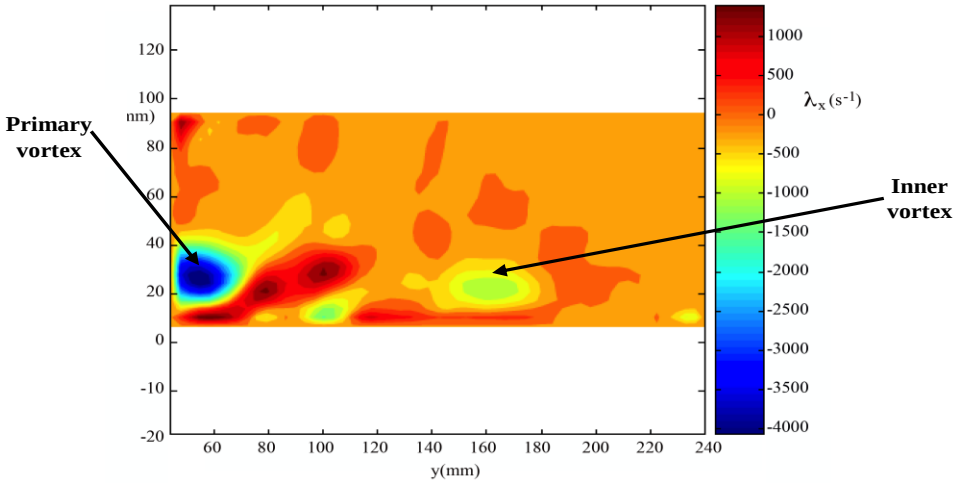

ii) Vorticity distribution

Fig. 11